JCND Special Issue on 2023 IDETC MSNDC Conference

Modeling of Vehicle Mobility in Shallow Water with Data-Driven Hydrodynamics Model

Hiroki Yamashita
Juan Ezequiel Martin
University of Iowa, Iowa City, IA 52242

Nathan Tison
Arkady Grunin
Paramsothy Jayakumar
U.S. Army DEVCOM GVSC, Warren, MI 48397

*Hiroyuki Sugiyama**
Department of Mechanical Engineering
University of Iowa, Iowa City, IA 52242
**hiroyuki-sugiyama@uiowa.edu*

DISTRIBUTION STATEMENT A. Approved for public release; distribution is unlimited. OPSEC #: 7983

ABSTRACT

In this study, a numerical procedure for predicting vehicle mobility in shallow water is proposed with the data-driven hydrodynamics model, considering the effect of soil deformation. To this end, the high-fidelity coupled CFD-MBD model is developed to characterize the hydrodynamic loads exerted on the vehicle in shallow water and used to generate the training dataset for the proposed data-driven model. To account for the history-dependent hydrodynamic force and moment characteristics, LSTM is introduced to account for the effect of the historical variation of the vehicle motion states as the input to the data-driven model. The data-driven models are called from the MBD mobility solver at every time step to determine the hydrodynamic loads, allowing for predicting the transient responses of the vehicle interacting with shallow water on deformable soil. It is demonstrated by several numerical examples that the complex vehicle-water interaction behavior was predicted accurately by the proposed data-driven hydrodynamics model while achieving a substantial computational speedup. The predictive ability and computational benefit of the proposed hybrid LSTM-MBD vehicle-water interaction model are demonstrated.

1. INTRODUCTION

Off-road ground vehicles are operated in highly complex environments, including water fording and river crossings. Accurate vehicle mobility prediction in shallow water, therefore, plays a critical role in reliable mission planning [1] and autonomous navigation [2]. However, only limited studies have been conducted due to the difficulties in predicting the vehicle-water interaction, which requires integration of the high-fidelity computational fluid dynamics (CFD) and multibody dynamics (MBD) solvers [3-7]. The coupled CFD-MBD simulations have high computational costs, making it prohibitive to run many simulations to evaluate vehicle maneuverability in stochastic water and terrain conditions, construct mobility maps, and tune control parameters for navigation algorithms. The use of computationally efficient reduced-order hydrodynamics models can circumvent this limitation. Such an approach is currently used for other applications, including simulations of autonomous underwater vehicles [8,9]. In indicial reduced-order models, the resultant hydrodynamic forces, accounting for the effect of the water resistance, damping, added mass, propulsion, etc., are approximated as a function of the vehicle velocity with many regression coefficients, which need to be identified under various vehicle and water conditions. These hydrodynamic coefficients are defined by polynomials of the vehicle and environmental parameters to replicate the hydrodynamic load characteristics obtained by the high-fidelity CFD model. Whereas such a coefficient-based reduced order model can lower the model complexity, it requires many simulation runs with the high-fidelity CFD model to cover a wide range of operational conditions. Most importantly, history effects are neglected, as the coefficients are identified in steady conditions. Furthermore, coupling effects of hydrodynamic loads cannot be properly captured. That is, in ground vehicle applications, the wheel and chassis (hull) resistances are added as independent quantities, and their coupling (interaction) is not considered if the

resistance for the chassis (hull) is calculated without turning wheels for all flow and vehicle maneuvering conditions.

On the other hand, data-driven modeling approaches have drawn increasing attention in scientific computing to address the high computational intensity of CFD simulations [10-18]. In particular, deep neural networks are utilized to model the flow dynamics and to enhance CFD. For example, velocity fields predicted by a fine mesh CFD model are learned by a deep neural network to enhance accuracy of a coarse mesh CFD model [12]. Machine learning techniques are also leveraged to learn solutions of ordinary and partial differential equations. Among others, there are many studies on data-driven prediction of the time-domain response of reduced order coordinates associated with the truncated proper orthogonal decomposition (POD) modes of flow fields obtained from CFD [13-16]. This leads to a data-driven model order reduction (MOR), in which the computationally expensive time integration process is replaced by deep neural networks. Data-driven prediction of a body motion, resulting from the interaction with water, is also explored. For example, in ship hydrodynamics, the heave, pitch, and roll responses to wave elevation inputs are predicted by Long Short-Term Memory (LSTM) neural networks [17,18]. However, in the context of the vehicle-water interaction, inputs to the neural network should include the wheel steering and speed variations, traction/braking, and water conditions. Thus, direct vehicle motion prediction by deep learning necessitates a significant amount of training data, which has to be generated by computationally expensive high-fidelity models.

Therefore, this study explores a data-driven prediction of the hydrodynamic loads, which can be fully integrated into the multibody dynamics simulation framework, to enable quick and accurate prediction of vehicle maneuverability in shallow water. Since the vehicle motion is predicted by the physics-based MBD vehicle model subjected to the data-driven hydrodynamic

loads, the vehicle transient response can be obtained accurately by the mobility solvers without reliance on the pure data-driven approach. Furthermore, since a high-fidelity coupled CFD-MBD model, accounting for the transient vehicle-water interaction, is developed and used to generate training data for the data-driven hydrodynamics model, the dynamic coupling effects of the hydrodynamic loads can be automatically incorporated in the proposed data-driven hydrodynamics model.

2. COUPLED CFD-MBD SIMULATION FRAMEWORK

A high-fidelity computational model for vehicle-water interactions in shallow water is developed by leveraging the coupled CFD-MBD simulation capability [7].

2.1 Computational Fluid Dynamics Solver

The CFD solver used in this study is REX developed at the University of Iowa. REX is a structure, multigrid, free surface, and incompressible CFD solver primarily developed for naval applications [19-22]. Dynamic overset interpolation is used to resolve grid motions. Control, propulsion and full six degrees-of-freedom (6DOF) rigid-body motion computations with moving control surfaces are available natively in the code. Details of the code are given in the referenced literature, and only a brief overview is presented in this section.

REX is an unsteady Reynolds-averaged Navier-Stokes (URANS) solver with multiple available turbulence closure models. The basic mass and momentum conservation equations are given by

$$\frac{\partial u_j}{\partial x_j} = 0 \tag{1}$$

$$\frac{\partial u_i}{\partial t} + \frac{\partial u_i u_j}{\partial x_j} = -\frac{\partial p}{\partial x_i} + \frac{\partial}{\partial x_j}\left[\frac{1}{\mathrm{Re}_{eff}}\left(\frac{\partial u_i}{\partial x_j} + \frac{\partial u_j}{\partial x_i}\right)\right] + s_i \tag{2}$$

where u is the dimensionless water velocity, x is the dimensionless coordinate, p is the dimensionless dynamic pressure, and s_i is a body force (for instance, propulsion). The equations are non-dimensionalized with the arbitrary nominal velocity U_0 and vehicle length L_0. The dimensionless piezometric pressure is defined as $p = \hat{p} / \rho U_0^2 + 2k/3$, where $\hat{p}$ is the pressure, ρ is the density, and k is the turbulent kinetic energy. One also has $1/\mathrm{Re}_{eff} = 1/\mathrm{Re} + \nu_t$, where Re_{eff} is the effective Reynolds number and ν_t is the turbulent viscosity obtained from a turbulence model. Overset connectivity is computed at each timestep using the third-party software Suggar++ [23], which allows for arbitrary motion of the different grids to simulate the motions of immersed bodies. Overset connectivity on the body surface, including panel weighting for overlapping cells also allows the accurate integration of pressure and viscous forces acting on the body. The overset approach also allows the implementation of immersed boundaries required for the contact problem in the vehicle-terrain interaction [7].

2.2 Multibody Off-Road Mobility Solver

A general-purpose multibody dynamics solver, IMBD, is used to predict vehicle motion on deformable soil, and it is coupled with REX through a co-simulation coupling algorithm. IMBD has unique tire-soil interaction simulation capabilities for high-fidelity off-road vehicle mobility prediction with a scalable high-performance computing scheme [24-29]. The deformable tire is modeled by nonlinear composite shell elements based on the absolute nodal coordinate formulation (ANCF), while complex granular terrain behavior can be modeled using the hierarchical multiscale modeling approach. In this approach, the macro-scale soil deformation is modeled by the continuum-based finite element (FE) or material point methods (MPM), while the grain-scale inter-particle soil material behavior at every quadrature point is modeled by a

representative volume element (RVE) using the discrete element (DE) approach. Such a scale separation allows for efficient modeling of granular soil behavior, compared to pure DE models requiring a significant number of particles to describe not only the grain-scale soil behavior but also the macro-scale soil deformation [26]. The neural network surrogate model for the DE RVE enables substantial computational speedup for the hierarchical multiscale off-road mobility solver [28].

On the other hand, for fast off-road mobility simulations needed in developing and evaluating autonomous navigation algorithms considering stochastic terrain conditions, a simple terramechanics model based on the Bekker-Wong soil parameters is widely utilized [30-32]. In this approach, the basic soil material behavior is characterized by the soil pressure-sinkage and the shear stress-displacement curves given from experiments, thereby allowing for quick prediction of the soil sinkage as well as the tangential forces resulting from the interaction with deformable soil. As shown in Fig. 1, the radial normal soil pressure distribution on the contact surface is modeled as [30]

$$\sigma(\theta)=\begin{cases} r^r\left(\dfrac{k_c}{b}+k_\phi\right)\left(\cos\theta-\cos\theta_f\right)^n & \text{for } \theta_m\le\theta<\theta_f \\ r^r\left(\dfrac{k_c}{b}+k_\phi\right)\left(\cos\left(\theta_f-\dfrac{\theta-\theta_r}{\theta_m-\theta_r}(\theta_f-\theta_m)\right)-\cos\theta_f\right)^n & \text{for } \theta_r\le\theta\le\theta_m \end{cases} \tag{3}$$

where r and b are the wheel radius and width; k_c and k_ϕ are fitting parameters associated with the soil cohesion and friction angle; and n is an exponent of the power function to define the degree of nonlinearity of the pressure-sinkage curve. These parameters are calibrated to produce the pressure-sinkage curves that match the lab or in-situ soil test data. The radial coordinate θ defined from the vertical axis intersecting the wheel center gives a point on the contact surface. The maximum pressure point is given by θ_m, and its location depends on the longitudinal slip [31].

The front and rear edges of the contact patch are given by θ_f and θ_r, respectively.

The tangential stress at θ on the contact surface is approximated by [30]

$$\tau_i(\theta) = \tau_{\max}(1 - e^{-j_i(\theta)/k}) \text{ for } i = x \text{ and } y \tag{4}$$

where $\tau_{\max}$ is the soil strength based on the Coulm-Mohr failure criterion, and it is given by $\tau_{\max} = c + \sigma(\theta)\tan\phi$ (Coulomb-Mohr failure line), where c is the soil cohesion and ϕ is the soil friction angle. k_i is the fitting parameter that characterizes the slope of the shear stress-displacement curve in the longitudinal ($i = x$) and lateral ($i = y$) directions. The shear displacement at the radial coordinate θ is given by j_i (i = x and y) [31]. Using the assumed pressure distribution $\sigma(\theta)$ along with the tangential surface traction $\tau_x(\theta)$ and $\tau_y(\theta)$, the resultant longitudinal, lateral, and vertical forces exerted on the tire contact zone from the deformable soil can be, respectively, defined by

$$\left.\begin{aligned} F_x &= rb\int_{\theta_r}^{\theta_f} (\tau_x(\theta)\cos\theta - \sigma(\theta)\sin\theta)d\theta \\ F_y &= rb\int_{\theta_r}^{\theta_f} \tau_y(\theta)d\theta \\ F_z &= rb\int_{\theta_r}^{\theta_f} (\tau_x(\theta)\sin\theta + \sigma(\theta)\cos\theta)d\theta \end{aligned}\right\} \tag{5}$$

To develop a fast vehicle-water interaction simulation model, considering soil deformation, the simple terramechanics model is incorporated into the coupled CFD-MBD simulation framework and used in this study.

The generalized force vector for the preceding tire-soil interaction forces is calculated and added to the right-hand side of the equations of motion for a vehicle system as follows:

$$\left.\begin{aligned} &\mathbf{M}_r\ddot{\mathbf{q}}_r + \mathbf{C}_{\mathbf{q}_r}^T\boldsymbol{\lambda} = \mathbf{Q}_r + \mathbf{Q}_{\text{hyd}} \\ &\mathbf{C}(\mathbf{q}_r, t) = \mathbf{0} \end{aligned}\right\} \tag{6}$$

where the generalized coordinates of the rigid multibody vehicle components are given by $\mathbf{q}_r$, while the mechanical joints, as well as prescribed motion trajectories for the vehicle components, are defined by the kinematic constraint equations $\mathbf{C}(\mathbf{q}_r, t) = \mathbf{0}$ and its Jacobian matrices are defined by $\mathbf{C}_{\mathbf{q}_r} = \partial \mathbf{C} / \partial \mathbf{q}_r$. The Lagrange multipliers associated with the constraint equations are given by the vector $\boldsymbol{\lambda}$. The tire-soil interaction forces are included in the generalized external force vector $\mathbf{Q}_r$, while the generalized hydrodynamic forces given from CFD through the co-simulation coupling process are given by $\mathbf{Q}_{\text{hyd}}$.

2.3 Coupled CFD-MBD Co-Simulation Framework

The coupled co-simulation framework is implemented in a parallel computing environment, using the Message Passing Interface (MPI). The co-simulation requires the exchange of data between the two solvers, the explicit forces and displacements, as shown in Fig. 2. The generalized coordinates and velocities of the multibody vehicle model are transferred to the CFD solver every macro time step, where the extrapolated data are generated to estimate the vehicle configurations at future time steps, as needed for the overset connectivity calculation in CFD. Since the extrapolated generalized coordinates and velocities may violate the constraint equations, the geometric constraint projection is performed, and the extrapolated data are projected on the constraint manifold to enforce the kinematic constraints for the interconnected multibody vehicle model [7]. The CFD can then predict the hydrodynamic forces and moments in the current vehicle motion state provided by the MBD solver. The equations of motion for the multibody vehicle model considering the generalized hydrodynamic forces $\mathbf{Q}_{\text{hyd}}$ (Eq. 6) are then integrated forward in time until the next macro step is reached. This process is repeated every macro time step to obtain the transient vehicle responses in shallow water.

3. DATA-DRIVEN HYDRODYNAMICS MODEL

Although accurate solutions can be obtained from the high-fidelity coupled CFD-MBD models, the computational cost is very high, and they are not suited for the analysis which requires many simulation runs, including evaluation of vehicle maneuverability in stochastic water and terrain conditions, construction of mobility maps, tuning of control parameters for navigation algorithms, etc. Therefore, to develop a fast computational model capable of predicting vehicle mobility in shallow water, a surrogate model for the high-fidelity hydrodynamic loads obtained from the coupled CFD-MBD solver is proposed, considering multiple environmental and vehicle variables and the effect of soil deformation.

To this end, neural network surrogate models are constructed to predict the hydrodynamic forces and moments ($\mathbf{F}_{\text{hyd}}$ and $\mathbf{N}_{\text{hyd}}$) for the hull and tire/suspension components, given their motion states and water condition every time step, as summarized in Fig. 3. The vehicle and water states are characterized by the sideslip angle (α) defining the lateral slip of the body of interest given by an angle between the longitudinal velocity vector and the body heading axis; the angle of attack (β) defining the angle between the water flow and the body heading axis; the vehicle speed V; water speed U_w; and water depth D_w, as shown in Fig. 4. For body i, the following state variables are defined at time t_n:

$$\mathbf{y}^i(t_n) = [\alpha^i(t_n) \quad \beta^i(t_n) \quad V^i(t_n) \quad U_w^i(t_n) \quad D_w^i(t_n)]^T \tag{7}$$

One can add more inputs, including soil parameters for different soil conditions. It is worth noting here that the hydrodynamic load response is influenced by the state history of the vehicle and water; thus the neural network becomes less predictive if the historical variation of the input state variables is not considered. Thus, a Long Short-Term Memory (LSTM) neural network [33] is introduced to account for the effect of the sequential variation of the state variables on the

hydrodynamic forces and moments for each body. An LSTM contains recurrent units in its hidden layers, which allow for maintaining information in long and short-term memories over time. Given the input vector x_t, the current LSTM output h_t and the cell state c_t can be obtained with the previous outputs h_{t-1} and c_{t-1}. They are written in a compact form as [33]

$$h_t = o_t * \tanh c_t \quad \text{and} \quad c_t = f_t * c_{t-1} + i_t * \tilde{c}_t \tag{8}$$

where * indicates element-wise product, and f_t, i_t, o_t and $\tilde{c}_t$ are given by

$$\left.\begin{aligned} o_t &= S(W_o x_t + U_o h_{t-1} + b_o) \\ f_t &= S(W_f x_t + U_f h_{t-1} + b_f) \\ i_t &= S(W_i x_t + U_i h_{t-1} + b_i) \\ \tilde{c}_t &= \tanh(W_c x_t + U_c h_{t-1} + b_c) \end{aligned}\right\} \tag{9}$$

Note that *S* in Eq. 9 indicates a sigmoid function. W_l and U_l are weight matrices, and b_l is a bias vector. These weights and biases for $l = o, f, i$ and c in Eq. 9 are learned through training. Since LSTM can process sequential data and predict output in the future step, it has been utilized to forecast sequential responses in various applications [34]. In the present data-driven model, the input state vector in the current and previous two steps (i.e., $\mathbf{y}^i(t_n)$, $\mathbf{y}^i(t_{n-1})$ and $\mathbf{y}^i(t_{n-2})$) are considered to predict the hydrodynamic forces and moments of body *i* every time step (i.e., $t = t_n$), where the hydrodynamic load outputs are defined in its body coordinate system as

$$\left.\begin{aligned} \bar{\mathbf{F}}^i_{\text{hyd}}(t_n) &= [\bar{F}^i_{\text{x}}(t_n) \quad \bar{F}^i_{\text{y}}(t_n) \quad \bar{F}^i_{\text{z}}(t_n)]^T \\ \bar{\mathbf{N}}^i_{\text{hyd}}(t_n) &= [\bar{N}^i_{\text{x}}(t_n) \quad \bar{N}^i_{\text{y}}(t_n) \quad \bar{N}^i_{\text{z}}(t_n)]^T \end{aligned}\right\} \tag{10}$$

where the global force and moment vectors can be obtained using the rotation matrix $\mathbf{A}^i$ of body *i* as $\mathbf{F}^i_{\text{hyd}} = \mathbf{A}^i \bar{\mathbf{F}}^i_{\text{hyd}}$ and $\mathbf{N}^i_{\text{hyd}} = \mathbf{A}^i \bar{\mathbf{N}}^i_{\text{hyd}}$.

Training data are produced using the high-fidelity CFD-MBD vehicle model for various training scenarios. As shown in Fig. 3, the trained neural networks are called from the force module

of the multibody off-road mobility solver to define the hydrodynamic loads in the time integration process. That is, the data-driven model is utilized as a force function in the multibody dynamics simulation algorithm to account for the hydrodynamics effects of the vehicle traveling in shallow water. The predicted body forces and moments at the current time step are added to the right-hand side of the equations of motions as $\mathbf{Q}_{\text{hyd}}$ in Eq. 6. Having obtained the generalized coordinates and velocities at the next time step through the time integration process, the latest input state variables are updated and fed into the LSTM input for the future time step. This process is repeated until the final time step is reached.

4. VEHICLE LANE CHANGE MANEUVER IN SHALLOW WATER USING HIGH-FIDELITY COUPLED CFD-MBD MODEL

Numerical examples are presented to discuss the vehicle cornering behavior in shallow water, considering deformable soil, using a model-scale vehicle based on a leisure amphibious vehicle shown in Fig. 3 [7, 35]. The vehicle has a total weight of 57 kg, ground clearance of 78 mm, and wheelbase of 714 mm. A single lane change maneuver in shallow water is performed, in which the vehicle travels against an incoming flow. The wheel steering angle input is given as shown in Fig. 5, and a constant angular velocity of 10 rad/s is prescribed for the four tires. The Bekker-Wong soil parameters from the in-situ soil tests in the literature [36] are utilized to account for the effect of soil deformation. Figure 6 shows the vehicle trajectories obtained from the coupled CFD-MBD simulation for different water depths and speeds. The time integration stepsizes (i.e., *micro* stepsizes) for the CFD and MBD solvers are, respectively, 1 ms and 0.1 ms, while the CFD and MBD communication stepsize (i.e., *macro* stepsize) is 1 ms. Although the MBD stepsize is smaller than the CFD stepsize, most computational cost is taken up by the CFD. The water depth is defined by a ratio of the water height to the tire diameter of the vehicle, and 40% and 60% water depths

are considered in the vehicle trajectory results presented in Fig. 6. The water speeds of 0 m/s (calm water) and 1 m/s are considered to examine the effect of incoming water flow. The result without considering the effect of water is also presented by the dashed line in Fig. 6 for comparison, where the same soil parameters are used to examine the effect of water on the vehicle cornering behavior.

In the calm water condition with 60% water depth (D60/U0), the vehicle successfully performs the lane change maneuver, while the vehicle lateral displacement after completing the lane change maneuver is smaller than that without water. This is attributed to the fact that the vehicle speed attained in the water, given the prescribed wheel angular speeds, is lowered due to the motion resistance from water and the loss of the wheel loads by buoyancy. This results in a shorter traveling distance when considering the interaction with water. The hydrodynamic forces and moments exerted on the hull defined with respect to the body coordinate system are shown in Fig. 7, where the negative longitudinal force, indicating the water resistance, is applied to the vehicle, while the positive vertical force, indicating the net buoyancy, is applied to the hull. These hydrodynamic loads contribute to altering the vehicle trajectory from that in the no water condition.

When considering an incoming water flow of 1 m/s with the same water depth (D60/U1), the vehicle is considerably shifted laterally, resulting in the vehicle trajectory being drifted from the ideal path, as shown in Fig. 6. Furthermore, the traveling distance of the first straight part is much shorter than that in the clam water condition (D60/U0), implying a significant loss of the net traction. This is attributed to the motion resistance from the incoming flow, as shown in Fig. 7. The vehicle is also subjected to the larger lateral hydrodynamic force and yaw moment, as observed from Fig. 7. Furthermore, variation of the roll and pitch moments becomes more significant due to the incoming water flow. These hydrodynamic effects negatively impact the vehicle cornering performance in this scenario. It is also observed from Fig. 8(b) that the vehicle

yaw angle in the D60/U1 condition does not return to zero after 5.5 s. Thus, the incoming water flow keeps pushing the yawed vehicle, resulting in the lateral velocity changing even after 5.5 s. On the other hand, the lateral velocity ideally returns to zero in the calm water condition (D60/ U0), as shown in Fig. 8(a).

When the water depth is decreased from 60% to 40% of the wheel diameter while keeping the flow speed 1 m/s (D40/U1), the lateral drifting behavior is significantly decreased, as shown in Fig. 6. In the lower water depth, the hull bottom surface slightly touches the water surface; thus the loss of the wheel loads by the buoyancy becomes smaller. As shown in Fig. 7, the buoyancy in D40/U1 is much smaller than that of D60/U1 due to the shallower water depth (D40), allowing for the vehicle to navigate without significant loss of the wheel traction even in the presence of the incoming flow.

Snapshots of the water free surface and the vehicle motion in D60/U0 and D60/U1 are shown in Fig. 9. Some notable characteristics of the resulting flow are the presences of larger wake and bow wave for D60/U1, which are consistent with the increased resistance, and asymmetry of the flow field in the traveling direction of the vehicle, except at straight ahead heading conditions at the beginning of the maneuver, that result in continuous lateral forces. Note that the maneuver fails in D60/U1 due to this asymmetry, as the turning action of the wheels has a much larger effect when turning with the flow against it. None of these effects are present in the calm water case, for which the effect of the water is mainly to increase resistance in the advance direction.

5. PREDICTION OF VEHICLE BEHAVIOR IN SHALLOW WATER USING DATA-DRIVEN HYDRODYNAMICS MODEL

5.1 Training of Data-Driven Hydrodynamics Model

Using the numerical results from the high-fidelity coupled CFD-MBD model presented in Section 4, the LSTM data-driven hydrodynamics models are developed to enable fast prediction of the vehicle cornering behavior in shallow water, considering deformable soil, for various water depths and speeds. To this end, the parameter range for the target prediction scenarios is set to be 40%~60% water depths and 0~1 m/s water speeds. To cover these conditions, nine training scenarios with different combinations of the water depth and speed are selected as shown by circle symbols in Fig. 10, and the training data are generated accordingly. A set of the hydrodynamic forces and moments for the vehicle components are reorganized for five representative composite bodies: the hull and four tires with their suspension links. The resultant hydrodynamic forces and moments for each representative body are mapped with its input state variables (i.e., $\mathbf{y}^i(t_n)$, $\mathbf{y}^i(t_{n-1})$ and $\mathbf{y}^i(t_{n-2})$ for $i=1,\cdots,5$) to predict the output forces $\bar{\mathbf{F}}^i_{\text{hyd}}(t_n)$ and moments $\bar{\mathbf{N}}^i_{\text{hyd}}(t_n)$ at $t=t_n$. Each data-driven hydrodynamics model has a single LSTM layer with 400 neurons, followed by a dense layer with 100 neurons. Training is performed with the adaptive moment estimation (Adam) algorithm with a learning rate of 0.001. Figure 11 shows the vehicle trajectories predicted by the MBD model integrated with the LSTM data-driven hydrodynamics model for these training scenarios (solid lines). The results are compared with those of the high-fidelity couple CFD-MBD simulation (dashed lines), where the vehicle motions in the training water conditions are correctly reproduced with the data-driven hydrodynamics model embedded in the multibody vehicle mobility solver.

5.2 Prediction Results

To examine the predictive ability of the LSTM data-driven hydrodynamics model, the water depths and speeds not considered in the training dataset are selected, as shown by diamond symbols in Fig. 10: (1) D50/U0.5, (2) D60/U0.5, and (3) D50/U1. These water conditions are within the training data range. Figure 12 shows the vehicle trajectories for these prediction scenarios obtained by the MBD model with the LSTM hydrodynamics (solid lines). The predicted results are compared with the CFD-MBD simulation results (dashed lines). It is observed from this figure that the vehicle behaviors in the conditions not considered in the training dataset are predicted well with the data-driven hydrodynamics model. The vehicle lateral velocity and yaw angle in the prediction scenarios agree well with the CFD-MBD results considering deformable soil, as observed in Figs. 13(a) and (b), respectively. Furthermore, the vehicle steering angle input is decreased from 30 to 15 degrees for the D50/U0.5 scenario to examine whether the vehicle motion given by a steering input not considered in the training data can be predicted or not. As shown in Figs. 12 and 13, the 15-deg lane change vehicle behavior in the D50/U0.5 water condition is also very well predicted. Since the hydrodynamics loads are characterized by the vehicle and water state variables in the proposed data-driven model, rather than the vehicle motion inputs, the model is predictive as far as the range of the variation of the input state variables is covered by the training data. This allows for reducing the amount of training data, compared to a pure data-driven model, for which the vehicle motion needs to be directly predicted, given a variety of vehicle motion inputs under various water conditions.

The hydrodynamic forces and moments predicted during the MBD simulation by the data-driven model are presented in Fig. 14 for the D05/U1 scenario with the 30-degree steering angle. Although the small variation of the hydrodynamic loads are not captured, the dominant change in

the hydrodynamic forces and moments, which contribute to the vehicle cornering response, are well predicted over time. Such a prediction cannot be achieved by simple interpolation of the training data due to the highly nonlinear characteristics of the hydrodynamic forces and moments exerted on the multibody vehicle traveling over the complex deformable soil.

To examine the importance of considering the sequential inputs in the data-driven model to account for the history-dependent hydrodynamic force and moment behavior, the LSTM layer is replaced by the non-LSTM dense layer considering the input $\mathbf{y}^i(t_n)$ at only $t = t_n$ while keeping the number of neurons the same as the original LSTM layer. It is observed from Fig. 15 that the vehicle trajectories predicted by the non-LSTM data-driven hydrodynamics model deviate significantly from the coupled CFD-MBD simulation results, and the accuracy is not acceptable. Although the data-driven model can reproduce the vehicle responses in the training scenarios (i.e., fitting), the model is no longer predictive in the scenarios not considered in the training data, as the historical variation of the input state variables is not properly accounted for when predicting the hydrodynamic loads.

5.3 Computational Time

The computational time of each simulation was 1,099 seconds (18.3 minutes) with 28 processors used for evaluating multiple neural networks. On the other hand, the computational time of the original coupled CFD-MBD simulation was 73 hours (3 days) with 336 processors allocated for the CFD solver. A substantial computational speedup was achieved with the proposed data-driven hydrodynamics model, allowing for quick prediction of the vehicle behavior in shallow water successfully.

In these simulations, the macro stepsize is fixed to 1 ms as in the original coupled CFD-MBD simulation. In the hybrid LSTM-MBD vehicle-water interaction model, however, one can

select a larger macro stepsize as it is no longer limited by the CFD solver. It turned out that the MBD time integration stepsize can be increased to 0.5 ms, while the macro stepsize for calling the data-driven model was also increased to 20 ms without lowering the accuracy. This resulted in the overall computational cost being 214 seconds (3.5 minutes) in this example. It is worth noting here that one still needs to provide the LSTM input data (i.e., $\mathbf{y}^i(t_n)$, $\mathbf{y}^i(t_{n-1})$, and $\mathbf{y}^i(t_{n-2})$) at 1 ms interval even though the macro stepsize is greater than 1 ms, as the LSTM was trained with the sequential input given at every 1 ms. Since the MBD integration is performed with a stepsize smaller than 1 ms, the vehicle state variables updated at every MBD time integration step are used to define the sequential input for the LSTM hydrodynamics model.

6. SUMMARY AND CONCLUSIONS

Although high-fidelity coupled CFD-MBD simulations allow for predicting complex vehicle-water interaction accurately, the computational cost is very high, prohibiting many simulation runs required for the vehicle performance evaluation under stochastic terrain and water conditions, mobility map construction, parameter tuning for navigation algorithms, etc. To address the computational challenge in the high-fidelity coupled CFD-MBD simulation, this study proposed the data-driven hydrodynamic force and moment model to enable quick and accurate prediction of vehicle mobility in shallow water, considering deformable soil using the simple terramechanics model. The high-fidelity coupled CFD-MBD models were used to generate training data for the data-driven model replicating the hydrodynamic loads under various vehicle motion states. To account for the history-dependent hydrodynamic force and moment characteristics, LSTM was introduced to account for the effect of the historical variation of the vehicle motion states as the input to the data-driven model. The LSTM models were then called from the MBD off-road mobility solver to define the hydrodynamic loads on the vehicle components at every time step in

the time integration process.

Several numerical examples were presented to demonstrate the predictive ability and robustness of the LSTM data-driven hydrodynamics model that was fully integrated into the MBD mobility solver. The effect of water depths and incoming flow speeds on the vehicle cornering behavior in shallow water was examined using the high-fidelity coupled CFD-MBD model, showing the impacts of the hydrodynamic loads on the vehicle mobility capability in shallow water. Using the LSTM data-driven hydrodynamics model, it was demonstrated that the vehicle-water interaction behavior in the scenarios not considered in the training data was successfully predicted while capturing the history-dependent hydrodynamic loads, and the use of the non-LSTM layer in place of the LSTM led to inaccurate solutions. A substantial computational speedup was achieved while ensuring accuracy, compared to the computationally expensive high-fidelity coupled CFD-MBD model. The predictive ability and computational benefit of the proposed hybrid LSTM-MBD vehicle-water interaction model were successfully demonstrated.

ACKNOWLEDGEMENTS

This research is supported by the Automotive Research Center (ARC) in accordance with Cooperative Agreement W56HZV-19-2-0001 U.S. Army CCDC Ground Vehicle Systems Center (GVSC), Warren, MI.

DISCLAIMER

Reference herein to any specific commercial company, product, process, or service by trade name, trademark, manufacturer, or otherwise, does not necessarily constitute or imply its endorsement, recommendation, or favoring by the United States Government or the Department of the Army (DoA). The opinions of the authors expressed herein do not necessarily state or reflect those of the United States Government or the DoA, and shall not be used for advertising or product endorsement purposes.

REFERENCES

[1] Mechergui, D. and Jayakumar, P., 2020. Efficient generation of accurate mobility maps using machine learning algorithms. *Journal of Terramechanics*, 88, pp.53-63.

[2] Dallas, J., Cole, M.P., Jayakumar, P. and Ersal, T., 2021. Terrain adaptive trajectory planning and tracking on deformable terrains. IEEE Transactions on Vehicular Technology, 70(11), pp.11255-11268.

[3] Pazouki, A., Serban, R. and Negrut, D., 2014. A Lagrangian–Lagrangian framework for the simulation of rigid and deformable bodies in fluid. *Multibody Dynamics: Computational Methods and Applications* (pp. 33-52). Springer International Publishing.

[4] Wasfy, T.M., Wasfy, H.M. and Peters, J.M., 2015, August. Coupled multibody dynamics and smoothed particle hydrodynamics for modeling vehicle water fording. *International Design Engineering Technical Conferences and Computers and Information in Engineering Conference* (Vol. 57168, p. V006T10A076). American Society of Mechanical Engineers.

[5] Canelas, R.B., Brito, M., Feal, O.G., Domínguez, J.M. and Crespo, A.J.C., 2018. Extending DualSPHysics with a Differential Variational Inequality: modeling fluid-mechanism interaction. *Applied Ocean Research*, 76, pp.88-97.

[6] Tison, N., 2019. Wheeled Amphibious Vehicle Water Egress M&S Using CFD and Simplified Vehicle Modeling Methodologies. *Proceedings of the Ground Vehicle Systems Engineering and Technology Symposium* (pp. 13-15).

[7] Yamashita, H., Arnold, A., Carrica, P.M., Noack, R.W., Martin, J.E., Sugiyama, H. and Harwood, C., 2022. Coupled multibody dynamics and computational fluid dynamics approach for amphibious vehicles in the surf zone. *Ocean Engineering*, 257, p.111607.

[8] Banazadeh, A., Seif, M.S., Khodaei, M.J. and Rezaie, M., 2017. Identification of the equivalent linear dynamics and controller design for an unmanned underwater vehicle. *Ocean Engineering*, 139, pp.152-168.

[9] Martin, J.E., Hammond, M., Rober, N., Kim, Y., Cichella, V. and Carrica, P., 2022. Reduced order model of a generic submarine for maneuvering near the surface. *Symposium on Naval Hydrodynamics*, Washington DC, USA.

[10] Brunton, S.L., Noack, B.R. and Koumoutsakos, P., 2020. Machine learning for fluid mechanics. Annual Review of Fluid Mechanics, 52, pp.477-508.

[11] Vinuesa, R. and Brunton, S.L., 2022. Enhancing computational fluid dynamics with machine learning. *Nature Computational Science*, 2(6), pp.358-366.

[12] Kochkov, D., Smith, J.A., Alieva, A., Wang, Q., Brenner, M.P. and Hoyer, S., 2021. Machine learning–accelerated computational fluid dynamics. *Proceedings of the National Academy of Sciences*, 118(21), p.e2101784118.

[13] Hesthaven, J.S. and Ubbiali, S., 2018. Non-intrusive reduced order modeling of nonlinear problems using neural networks. Journal of Computational Physics, 363, pp.55-78.

[14] Wang, Z., Xiao, D., Fang, F., Govindan, R., Pain, C.C. and Guo, Y., 2018. Model identification of reduced order fluid dynamics systems using deep learning. International Journal for Numerical Methods in Fluids, 86(4), pp.255-268.

[15] Hong, S.H., House, A., Kaminsky, A.L., Tison, N., Ruan, Y., Korivi, V., Wang, Y. and Pant, K., 2021. Machine learning-based thermal and flow simulation on heterogeneous platform for signature

[16] Abadía-Heredia, R., López-Martín, M., Carro, B., Arribas, J.I., Pérez, J.M. and Le Clainche, S., 2022. A predictive hybrid reduced order model based on proper orthogonal

decomposition combined with deep learning architectures. *Expert Systems with Applications*, 187, p.115910.

[17] del Águila Ferrandis, J., Triantafyllou, M.S., Chryssostomidis, C. and Karniadakis, G.E., 2021. Learning functionals via LSTM neural networks for predicting vessel dynamics in extreme sea states. *Proceedings of the Royal Society A*, 477(2245), p.20190897.

[18] Xu, W., Maki, K.J. and Silva, K.M., 2021. A data-driven model for nonlinear marine dynamics. *Ocean Engineering*, 236, p.109469.

[19] Carrica, P.M., Wilson, R.V. and Stern, F., 2007. An unsteady single-phase level set method for viscous free surface flows. *International Journal for Numerical Methods in Fluids*, 53(2), pp.229-256.

[20] Huang, J., Carrica, P.M. and Stern, F., 2008. Semi-coupled air/water immersed boundary approach for curvilinear dynamic overset grids with application to ship hydrodynamics. *International Journal for Numerical Methods in Fluids*, 58(6), pp.591-624.

[21] Li, J., Yuan, B. and Carrica, P.M., 2020. Modeling bubble entrainment and transport for ship wakes: progress using hybrid RANS/LES methods. *Journal of Ship Research*, 64(04), pp.328-345.

[22] Carrica, P.M., Kerkvliet, M., Quadvlieg, F. and Martin, J.E., 2021. CFD simulations and experiments of a submarine in turn, zigzag, and surfacing maneuvers. *Journal of Ship Research*, 65(04), pp.293-308.

[23] Noack, R., Boger, D., Kunz, R.E. and Carrica, P., 2009. Suggar++: An improved general overset grid assembly capability. AIAA Paper 2009-3992, *19th AIAA Computational Fluid Dynamics*, San Antonio, TX.

[24] Yamashita, H., Jayakumar, P. and Sugiyama, H., 2016. Physics-based flexible tire model integrated with LuGre tire friction for transient braking and cornering analysis. *Journal of Computational and Nonlinear Dynamics*, 11(3), 031017.

[25] Yamashita, H., Jayakumar, P., Alsaleh, M. and Sugiyama, H., 2018. Physics-based deformable tire–soil interaction model for off-road mobility simulation and experimental validation. *Journal of Computational and Nonlinear Dynamics*, 13(2), 021002.

[26] Yamashita, H., Chen, G., Ruan, Y., Jayakumar, P. and Sugiyama, H., 2019. Hierarchical multiscale modeling of tire–soil interaction for off-road mobility simulation. *Journal of Computational and Nonlinear Dynamics*, 14(6), 061007.

[27] Yamashita, H., Chen, G., Ruan, Y., Jayakumar, P. and Sugiyama, H., 2020. Parallelized multiscale off-road vehicle mobility simulation algorithm and full-scale vehicle validation. *Journal of Computational and Nonlinear Dynamics*, 15(9), 091007.

[28] Chen, G., Yamashita, H., Ruan, Y., Jayakumar, P., Knap, J., Leiter, K.W., Yang, X. and Sugiyama, H., 2021. Enhancing Hierarchical Multiscale Off-Road Mobility Model by Neural Network Surrogate Model. *Journal of Computational and Nonlinear Dynamics*, 16(8), p.081005.

[29] Chen, G., Yamashita, H., Ruan, Y., Jayakumar, P., Gorsich, D., Knap, J., Leiter, K.W., Yang, X. and Sugiyama, H., 2023. Hierarchical MPM-ANN multiscale terrain model for high-fidelity off-road mobility simulations: A coupled MBD-FE-MPM-ANN approach. *Journal of Computational and Nonlinear Dynamics*, 18(7), p.071001.

[30] Wong, J.Y., 2022. *Theory of Ground Vehicles*. John Wiley & Sons.

[31] Ishigami, G., Miwa, A., Nagatani, K. and Yoshida, K., 2007. Terramechanics-based model for steering maneuver of planetary exploration rovers on loose soil. Journal of Field Robotics, 24(3), pp.233-250.

[32] Serban, R., Taves, J. and Zhou, Z., 2023. Real-time simulation of ground vehicles on deformable terrain. Journal of Computational and Nonlinear Dynamics, 18(8), p.081007.
[33] Hochreiter, S. and Schmidhuber, J., 1997. Long short-term memory. *Neural Computation*, 9(8), pp.1735-1780.
[34] Chollet, F., 2021. *Deep Learning with Python*. Simon and Schuster.
[35] Behara, S., Arnold, A., Martin, J.E., Harwood, C.M. and Carrica, P.M., 2020. Experimental and computational study of operation of an amphibious craft in calm water. *Ocean Engineering*, 209, p.107460.
[36] Letherwood, M., Jayakumar, P., Gerth, R. and Dasch, J., 2020. Cooperative demonstration of technology (CDT) for next-generation NATO reference mobility model (NG-NRMM). Tech. Rep., *North Atlantic Treaty Organization, Science and Technology Organization*, STO-TM-AVT-308.

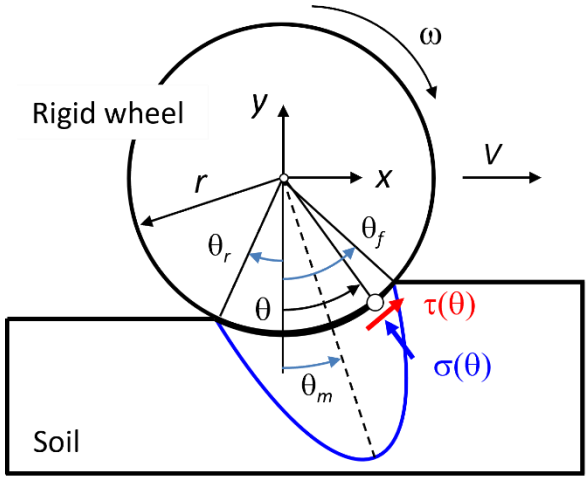

Figure 1 Tire-soil interaction model based on the Bekker-Wong soil parameters.

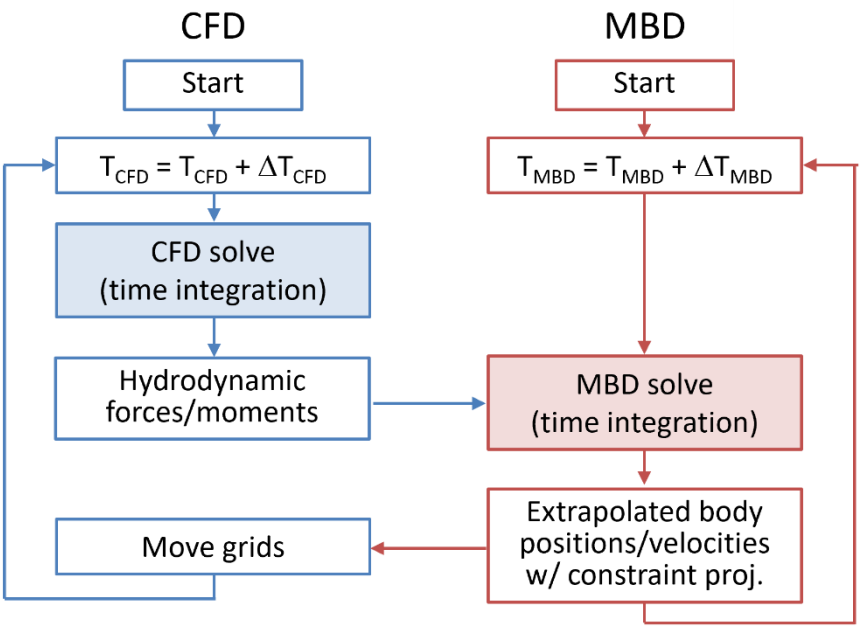

Figure 2 Co-simulation coupling procedure between CFD and MBD solvers.

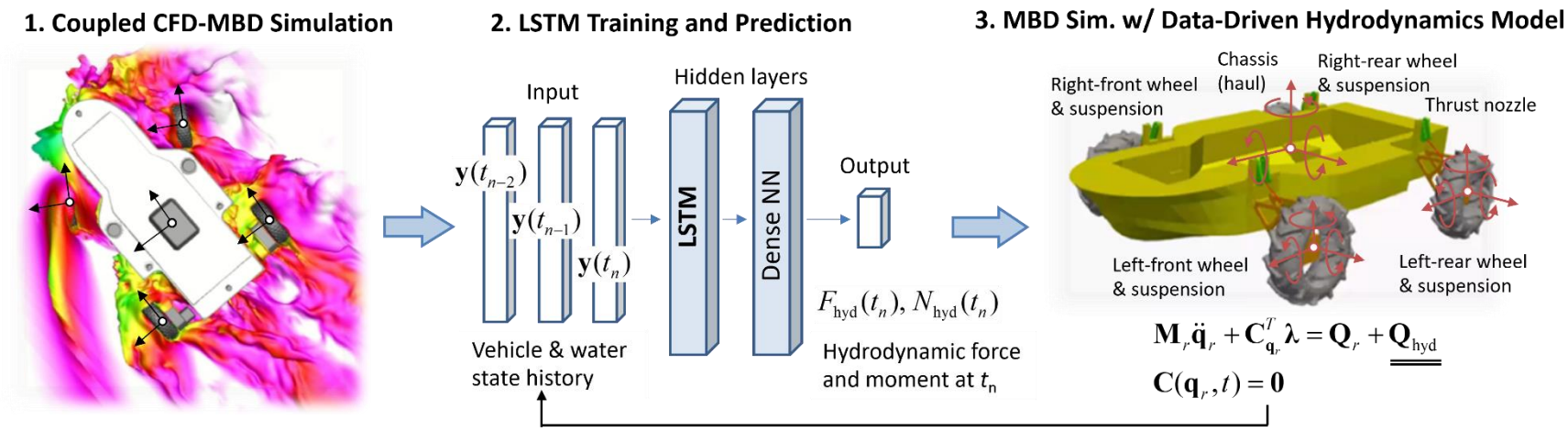

Figure 3 LSTM data-driven hydrodynamic force and moment model for vehicle-water interaction simulations.

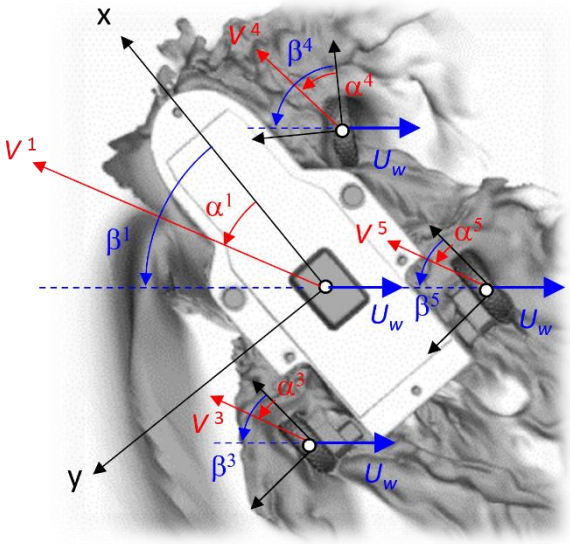

Figure 4 Definition of sideslip angle (α) and angle of attack (β) for vehicle bodies (hull and four tires with their suspension links) subjected to incoming water flow.

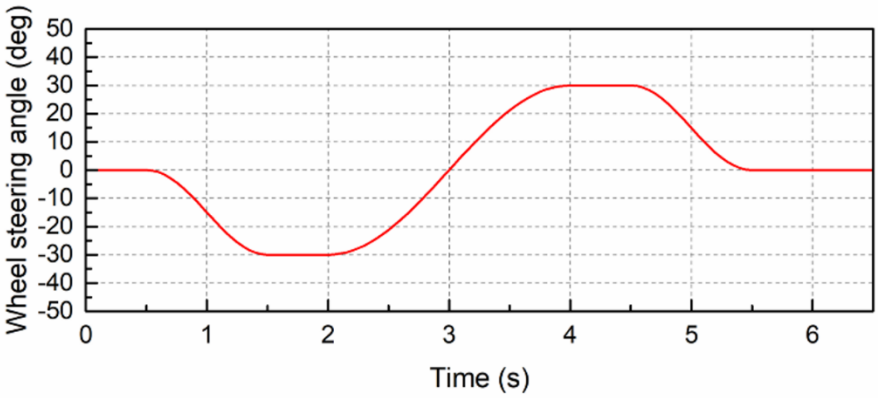

Figure 5 Wheel steering angle input for single lane change maneuver.

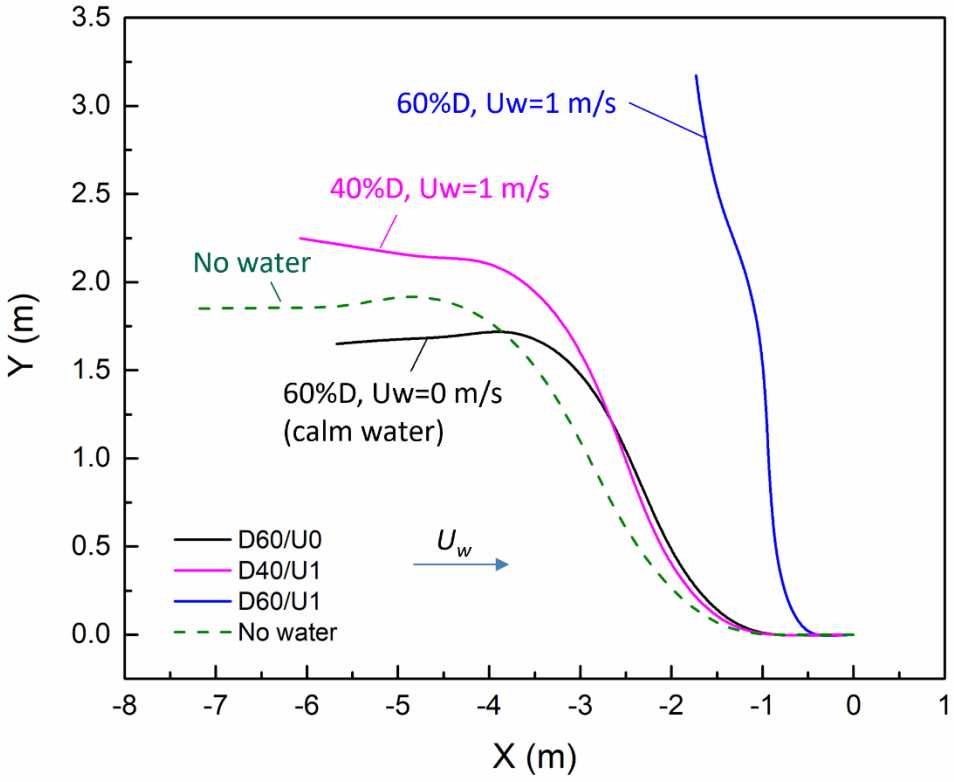

Figure 6 Vehicle trajectories obtained by the coupled CFD-MBD model.

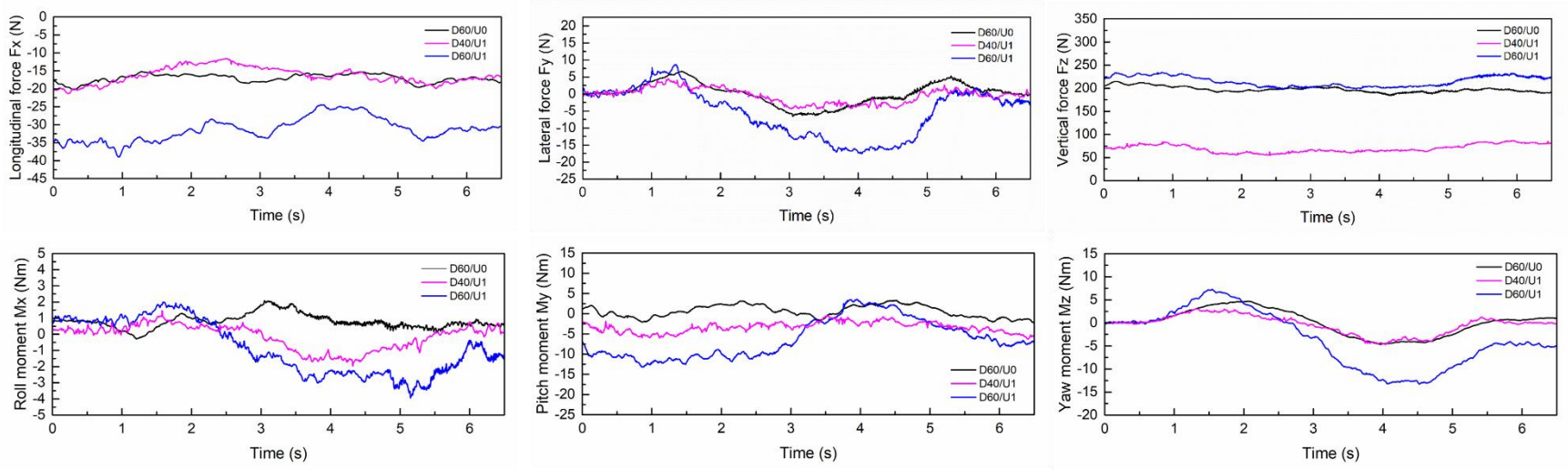

Figure 7 Hydrodynamic forces and moments exerted on the hull (chassis) predicted by the coupled CFD-MBD model.

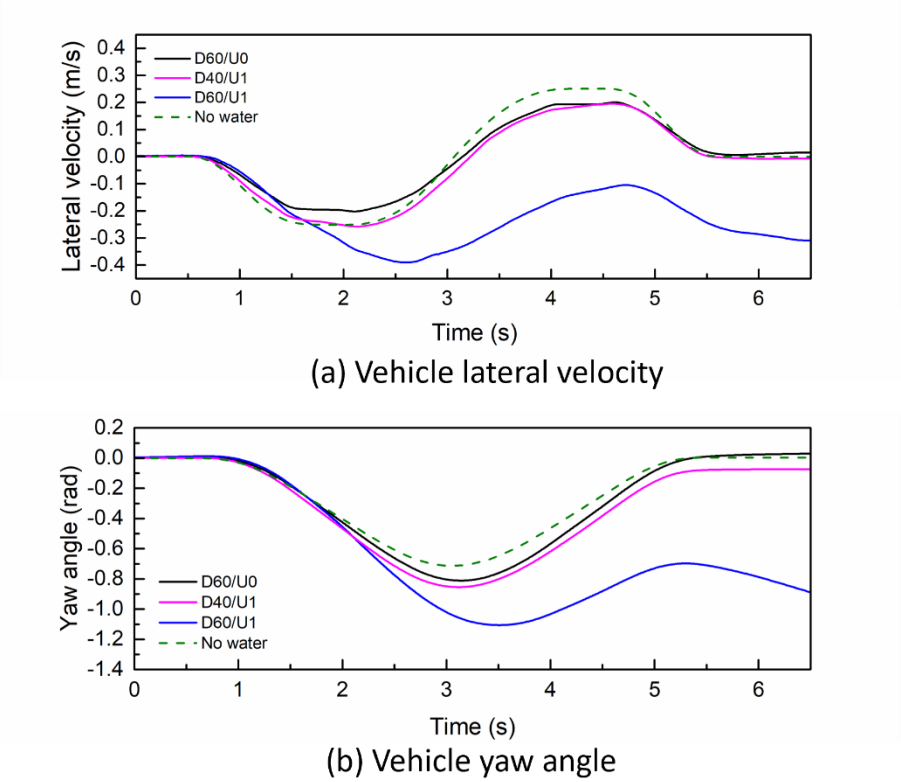

Figure 8 Vehicle lateral velocity and yaw angle obtained by the coupled CFD-MBD model.

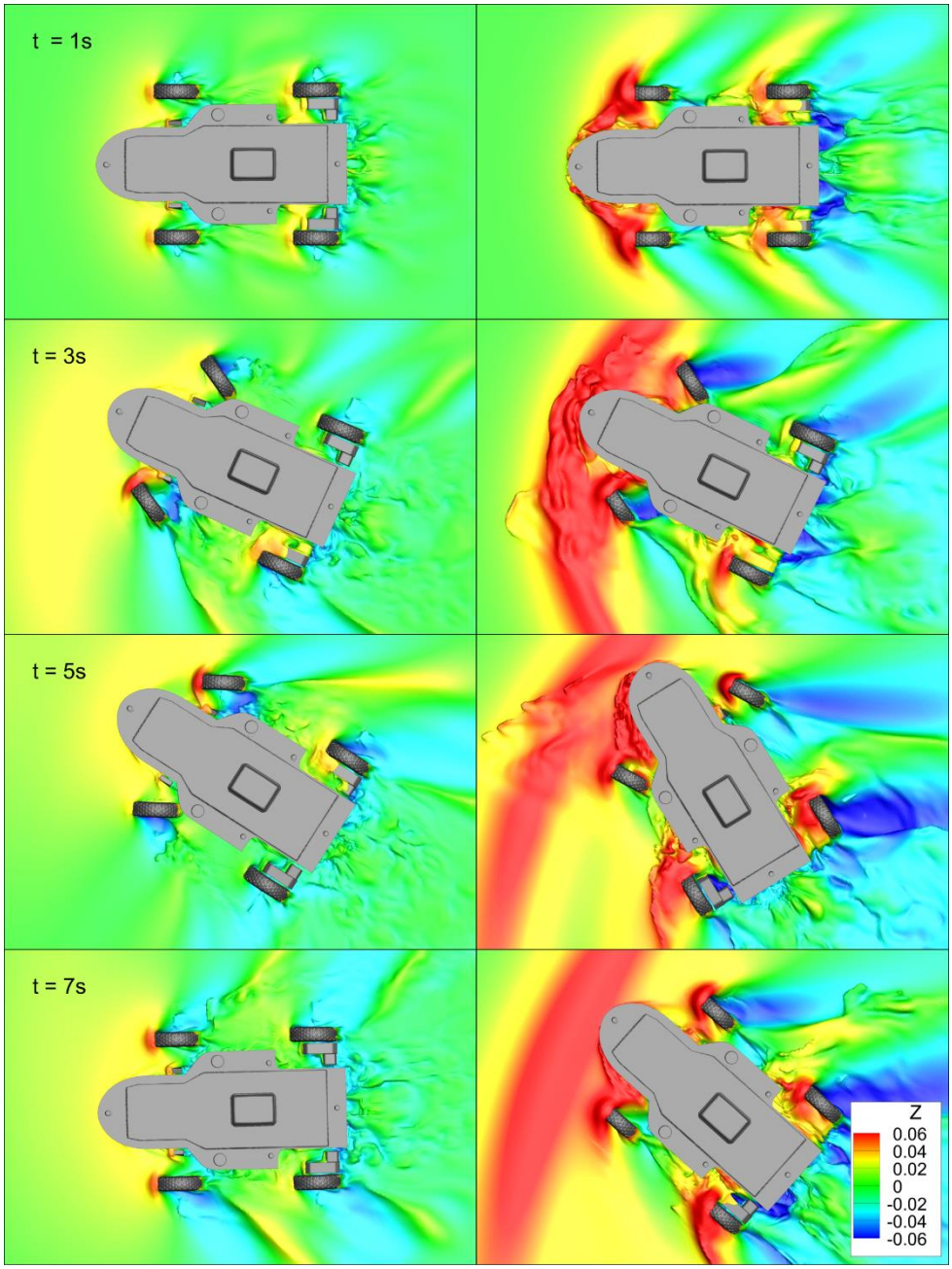

Figure 9 Water free surface and vehicle position for D60/U0 (left) and D60/U1 (right) at 2 second intervals. Free surface is colored by water elevation.

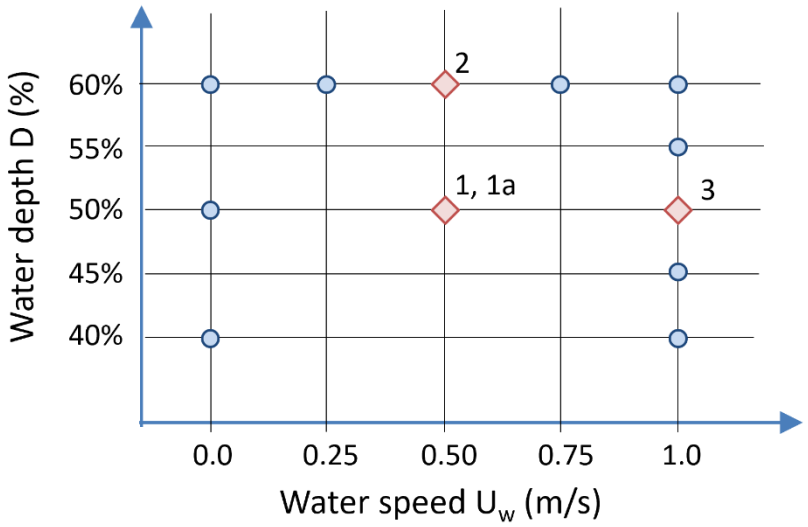

Figure 10 Water depth and speed for training and prediction scenarios. Training cases are shown by circle symbols, while the prediction cases are shown by diamond symbols.

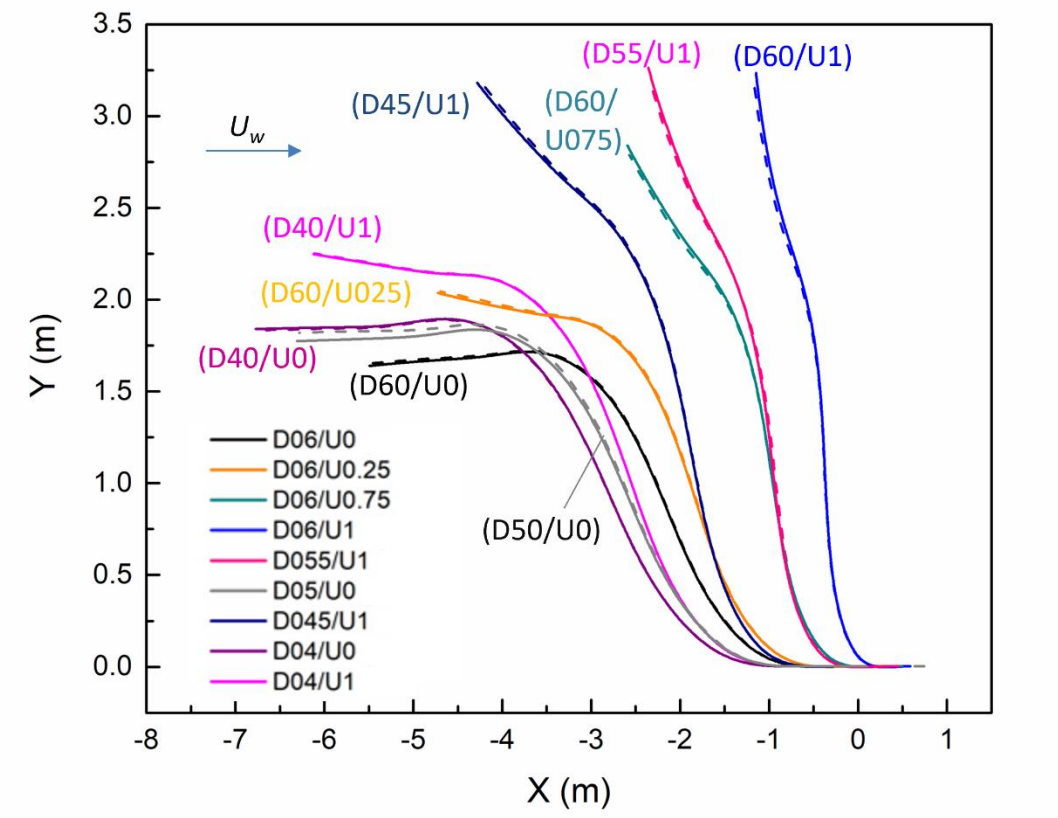

Figure 11 Vehicle trajectories in training scenarios predicted by the MBD model with the LSTM data-driven hydrodynamics model (solid lines). The results are compared with those of the coupled CFD-MBD model (dashed lines).

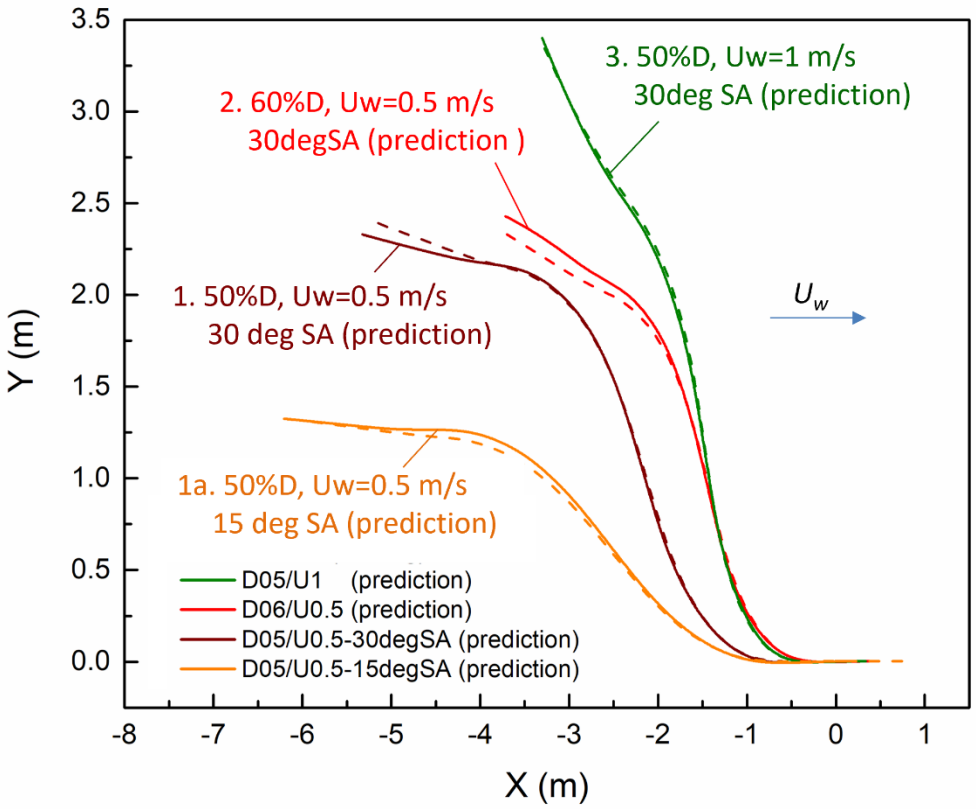

Figure 12 Vehicle trajectories in the scenarios not considered in the training data, predicted by the MBD model with the LSTM data-driven hydrodynamics model (solid lines). The results are compared with those of the coupled CFD-MBD model (dashed lines).

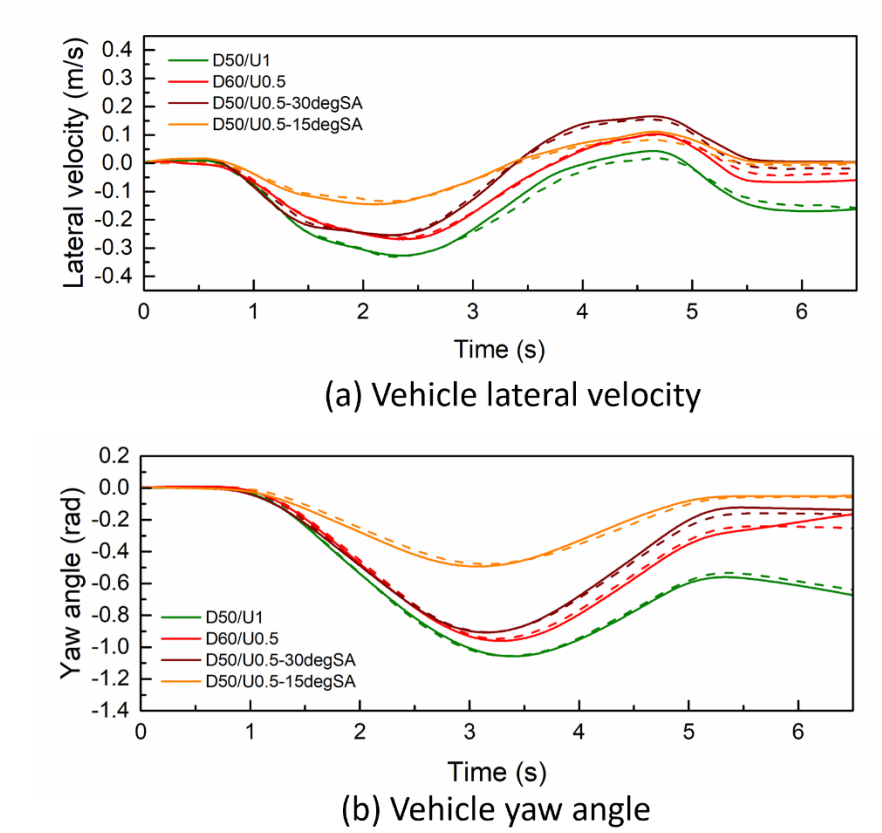

Figure 13 Vehicle lateral velocity and yaw angle in the scenarios not considered in the training data, predicted by the MBD model with the LSTM data-driven hydrodynamics model (solid lines). The results are compared with those of the coupled CFD-MBD model (dashed lines).

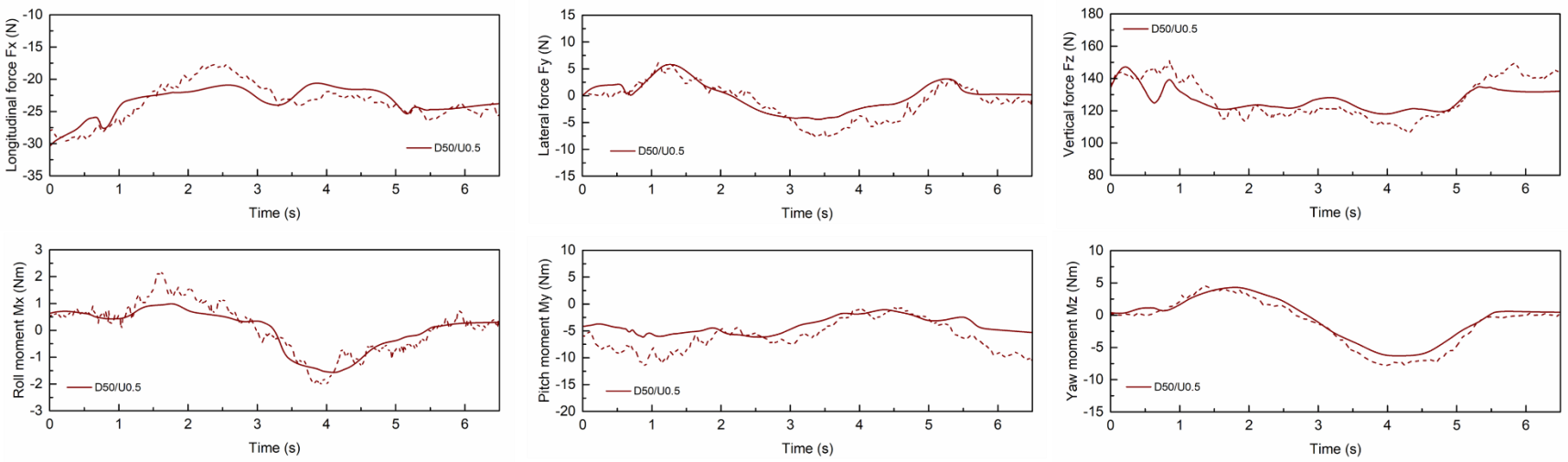

Figure 14 Hydrodynamic forces and moments exerted on the hull (chassis) in scenario D50/U0.5, predicted by the MBD model with LSTM data-driven hydrodynamics model (solid lines). The results are compared with those of the coupled CFD-MBD model (dashed lines).

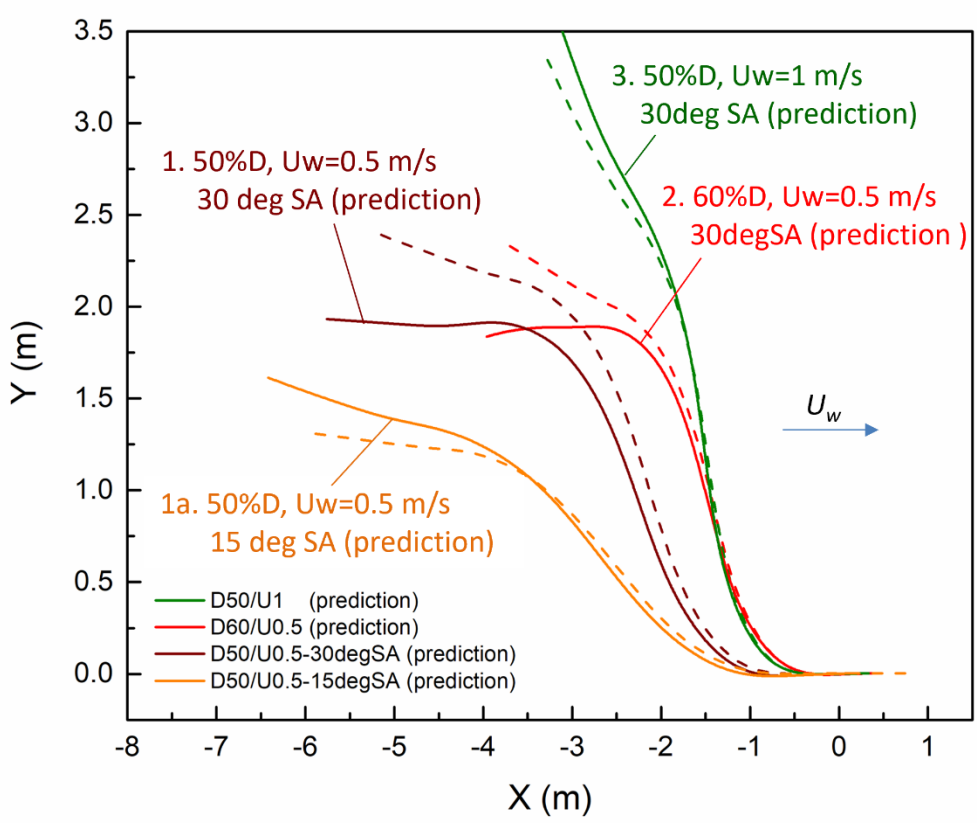

Figure 15 Vehicle trajectories in the scenarios not considered in the training data, predicted by the "non-LSTM" data-driven hydrodynamics model (solid lines). The results are compared with those of the coupled CFD-MBD model (dashed lines).